Fluidization-mediated tissue spreading by mitotic cell rounding and non-canonical Wnt signalling

Nicoletta I. Petridou [1], Silvia Grigolon [2], Guillaume Salbreux [2], Edouard Hannezo [1] and Carl-Philipp Heisenberg[1]

[1] Institute of Science and Technology Austria, Am Campus 1, 3400 Klosterneuburg, Austria

[2] The Francis Crick Institute, 1 Midland Road, London NW1 1AT, UK

Correspondence should be addressed to C.-P.H.

Tissue morphogenesis is driven by mechanical forces eliciting changes in cell size, shape and motion. The extent by which forces deform tissues critically depends on the rheological properties of the recipient tissue. Yet, whether and how dynamic changes in tissue rheology affect tissue morphogenesis, and how they are regulated within the developing organism remains unclear. Here we show that blastoderm spreading at the onset of zebrafish morphogenesis relies on a rapid, pronounced and spatially patterned tissue fluidization. Blastoderm fluidization is temporally controlled by mitotic cell rounding-dependent cell-cell contact disassembly during the last rounds of cell cleavages. Moreover, fluidization is spatially restricted to the central blastoderm by local activation of non-canonical Wnt signalling within the blastoderm margin, increasing cell cohesion and thereby counteracting the effect of mitotic rounding on contact disassembly. Overall, our results identify a fluidity transition mediated by loss of cell cohesion as a critical regulator of embryo morphogenesis.

Embryonic development is brought about by the integration of chemical and mechanical signals coordinating the transformation of an initially amorphous cell mass into a complex 3-dimensional organism [1,2]. Tissues intrinsically generate and/or extrinsically receive forces and deform in response to these forces depending on their dissipative properties, such as viscosity and elasticity [3,4]. Regulated changes in tissue material properties have previously been proposed to be important determinants for various morphogenetic processes in development, such as body axis elongation in zebrafish [5–7] and germ layer formation during *Xenopus* gastrulation [8,9]. Moreover, several cellular processes, such as cell adhesion, movement, and division, have been implicated in the regulation of tissue material properties [10–12]. Interestingly, while specific tissue material properties, such as tissue viscosity, have been shown to linearly scale with certain cellular properties, such as cell cohesion, this relationship is lost once a critical threshold level of cell cohesion is reached [10]. Likewise, theoretical considerations and studies on cultured cells have proposed that small changes in cell mechanical properties such as cell contractility and cell cohesion can lead to rapid, drastic and discontinuous changes in tissue rheology [13–16], driving tissue phase transitions such as solidification/jamming and fluidization. However, remarkably little is yet known about whether such abrupt and large changes in tissue rheology occur in animal development, how they are achieved on a molecular and cellular level, and, most importantly, what their function is within the developing embryo.

Here, we show that blastoderm spreading at the onset of zebrafish morphogenesis relies on a sharp transition of the tissue to a highly fluidized state. This tissue fluidization is triggered by a gradual decrease in cell cohesion, which is spatiotemporally controlled within the blastoderm by the concerted activities of cell cleavages and non-canonical Wnt signalling.

RESULTS

Blastoderm fluidizes at the onset of morphogenesis

At the onset of zebrafish development, the blastoderm, composed of deep cells covered by an epithelial enveloping layer (EVL), starts spreading over the yolk in a process called 'doming' [17,18] (**Fig. 1a-c**). During doming, the blastoderm-to-yolk interface (BYI) bends upwards in the centre and downwards at the margin reducing blastoderm height at the centre (**Fig. 1d, e; Supplementary Video 1**). These tissue shape changes have previously been attributed to two force-generating processes: active EVL expansion, reducing blastoderm tissue surface tension (TST), and active radial deep cell intercalations, radially contracting the blastoderm [19]. However, when mapping the spatiotemporal evolution of radial deep cell intercalations during doming, we noted that at the onset of doming (**Fig. 1b**) deep cell protrusions were not yet preferentially oriented along the radial axis of the blastoderm [19] (**Supplementary Fig. 1a, b**). This suggests that during doming initiation, radial stress generation might be minimal and, consequently, that other mechanisms besides active radial deep cell intercalations might be involved in initiating doming movements.

The timescale of tissue deformation generally depends on the relationship between active force generation and passive viscoelastic response [20]. We thus reasoned that reducing deep cell tissue resistance to active EVL expansion might constitute a mechanism by which blastoderm deformation is achieved when radial stress generation is minimal. To address this possibility, we performed stress-relaxation experiments using micropipette aspiration to map the material properties of the blastoderm deep cell tissue during doming (**Supplementary Fig. 1c-e**) [21,22]. We found that deep cell tissue viscosity sharply dropped (~10-fold) shortly before the onset of doming (**Fig. 1f** and **Supplementary Video 2**),

suggesting that the blastoderm fluidizes and becomes less resistant to force-induced deformation when doming sets in. Surprisingly, however, we also found that tissue fluidization was spatially restricted to central regions of the blastoderm and lasted only until dome stage, when the blastoderm tissue reaches a uniform thickness (**Fig. 1b, f**) and radial intercalations become more evident (**Supplementary Fig. 1a, b**). Together, this points to the intriguing possibility that a spatiotemporally restricted tissue fluidization facilitates blastoderm doming.

Tissue fluidization is essential for early blastoderm spreading

To test whether blastoderm fluidization is required for doming, we first developed a simplified model of blastoderm spreading where the deep cell tissue is represented as a passive fluid, subjected to an external force generated by EVL expansion driving its elongation (**Fig. 1g** and **Supplementary Fig. 1f**). Assuming that blastoderm volume is conserved [19], the fluid then constricts perpendicularly to the elongation axis (**Supplementary Note**). When the fluid viscosities were assumed to be equal, the fluid homogeneously constricted at a rate set by the elongation speed. In contrast, when assuming that viscosity is low only in the centre, reflecting our experimental observations, the central region constricted faster than the marginal region (**Fig. 1g, Supplementary Fig. 1g, h** and **Supplementary Video 3**). This suggests that selectively lowering blastoderm viscosity in the centre can in principle be sufficient to explain the increased rate of central tissue thinning observed in embryos with minimal radial stress generation. To quantitatively test this prediction, we turned to our fluid dynamic model of doming [19], where the blastoderm is described as an incompressible viscous fluid, the EVL as a two-dimensional expanding active fluid, the BYI and yolk-medium interface are subjected to a surface

tension, and the yolk has negligible viscosity (**Supplementary Note**). We asked whether the experimentally observed changes in blastoderm viscosity would be sufficient to achieve doming movements in embryos that undergo active EVL expansion, but lack radial stress generation (**Supplementary Note**). Selectively and strongly (~90%) reducing viscosity within the blastoderm centre, as observed in the aspiration experiments, led to blastoderm thinning along the symmetry axis that was considerably better matching the experimental observations than when assuming uniform high or low blastoderm viscosity (**Fig. 1h; Supplementary Table 1** and **Supplementary Video 4).** This suggests that spatially restricted fluidization of the blastoderm centre represents a plausible mechanism controlling blastoderm shape changes at the onset of doming when active force generation is largely restricted to EVL expansion.

To experimentally address the role of tissue fluidization in doming, we first asked whether fluidization of the central deep cell layer is tissue-autonomous. To this end, we prepared deep cell layer explants from the central blastoderm and analysed their viscoelastic properties *ex vivo*. Remarkably, we found that explants maintained the temporal pattern of viscosity changes as observed for the central blastoderm in intact embryos (**Fig. 1f** and **Supplementary Fig. 1c**), suggesting that deep cell tissue fluidization is a strictly tissue-autonomous process. Taking advantage of this, we performed heterotypic and heterochronic deep cell transplantation experiments to analyse the role of deep cell tissue fluidization in doming. In the heterotypic transplantations, we transplanted deep cells from the blastoderm margin of high stage donor embryos into the blastoderm centre of a high stage host embryo (**Fig. 2a**). In the heterochronic transplantations, we transplanted deep cells from the blastoderm centre of high stage donor embryos into the centre of the

blastoderm of a developmentally advanced host embryo (late sphere stage), in which tissue fluidization was about to start (**Fig. 2a**). As controls, we performed homotypic transplantations where we transplanted deep cells from the blastoderm centre of high stage donor embryos into the blastoderm centre of a high stage host embryo (**Fig. 2a**). Since fluidization is a deep cell tissue-autonomous process, we reasoned that in the heterotypic and heterochronic transplantations, the transplanted tissue would fail to undergo timely fluidization, allowing us to determine how local impairment of central tissue fluidization affects doming. In all cases, we confirmed through micropipette aspiration that the transplanted tissue retains its initial viscous properties (**Fig. 2d**). Interestingly, we found that in the heterotypic and heterochronic transplantations, where transplant fluidization was impaired, central blastoderm thinning at the position of the transplanted tissue was reduced, while no such effect was observed in the homotypic transplantations (**Fig. 2b, c** and **Supplementary Video 5**). This shows that interfering with central deep cell fluidization by either transplanting cells from the blastoderm margin or from embryos at pre-fluidization stages, affects central blastoderm thinning along its radial axis, suggesting that central blastoderm fluidization is required for proper doming movements.

To further test this notion, we interfered with tissue viscosity without varying cell origin and/or developmental stage. Specifically, we induced ectopic deep cell clustering by transplanting plastic beads coated with the ectodomain of E-cadherin into the blastoderm centre of a host embryo (**Supplementary Fig. 2a**), thereby locally increasing tissue viscosity (**Supplementary Fig. 2b**). In transplanted embryos, blastoderm thinning was reduced in the region of the transplant (**Supplementary Fig. 2c, d**), further supporting the notion that central tissue fluidization is needed for blastoderm doming.

Blastoderm tissue fluidization is mediated by de-stabilization of cell-cell contacts

To elucidate the molecular and cellular mechanisms by which tissue viscosity is selectively reduced in the blastoderm centre, we analysed cell cohesion throughout the blastoderm. We found that while at high stage both central and marginal deep cells displayed many stable and large cell-cell contacts (**Fig. 3a-d**), at the onset of doming central but not marginal cells gradually decreased their cell-cell contact number, duration and size, accompanied by increased interstitial fluid accumulations between them (**Fig. 3a-d**; **Supplementary Fig. 3a** and **Supplementary Video 6**). Notably, this difference in cell-cell contact dynamics and interstitial fluid distribution between central and marginal blastoderm regions mirrored their difference in tissue fluidity (**Fig. 1f**), suggesting that these phenomena might be functionally linked. To address this possibility, we first analysed the role of the interstitial fluid by examining blastoderm fluidity in *pky* mutant embryos which exhibit strongly reduced interstitial fluid accumulation and impaired osmolarity due to defective EVL differentiation and permeability at the onset of doming (**Supplementary Fig. 3b**) [23]. Interestingly, cell-cell contact dynamics and blastoderm fluidization in *pky* mutants were indistinguishable from wild type (WT) embryos (**Supplementary Fig. 3c, d**). Likewise, changing blastoderm osmolarity by exposing *pky* embryos to media with different osmolarity had no effect on blastoderm fluidization (**Supplementary Fig. 3d**). This suggests that changes in interstitial fluid accumulation and/or osmolarity within the blastoderm as such are unlikely to be the main determinants of deep cell-cell contact dynamics – at least to the extent analysed in this study – and associated blastoderm fluidization at the onset of doming.

To understand why central deep cells lose their contacts at the onset of doming, we first sought to identify the molecular and cellular processes leading to this loss. To this end, we isolated central and marginal deep cells and analysed their cell-cell contact dynamics *ex vivo*. Consistent with our observation of tissue-autonomous fluidization in central blastoderm explants (**Fig. 1f**), explanted central but not marginal deep cells gradually disassembled their cell-cell contacts in the same temporal pattern as observed *in vivo* (**Supplementary Fig. 3e**). This suggests that central deep cell-cell contact disassembly is caused by changes in the intrinsic cohesive properties of these cells. Further support for this notion also came from our observation that in the heterotypic and heterochronic transplantation experiments (**Fig. 2a**), the duration and size of cell-cell contacts between donor deep cells, which failed to trigger tissue fluidization, were selectively increased compared with the surrounding host deep cells (**Fig. 3e-g**).

To elucidate the molecular basis of the difference in cell-cell contact stability between central and marginal deep cells, we analysed the localization and distribution of cell-cell adhesion molecules. We found that E-cadherin [24,25] and associated cortical Actin accumulated at the contact edge between deep cells in both the central and marginal blastoderm at high stage (**Fig. 3h**). However, at the onset of doming no such distinct accumulation of E-cadherin and Actin was detectable anymore at cell-cell contacts within the blastoderm centre, while their junctional localization in marginal cells remained unchanged (**Fig. 3h**). Given that E-cadherin/Actin clustering at the cell-cell contact edge has previously been associated with stable cell-cell contacts [26], our findings suggest that cell-cell contact loss in the blastoderm centre at the onset of doming is due to intrinsic destabilization of E-cadherin-mediated cell-cell contacts.

Blastoderm tissue fluidization is temporally controlled by the cleavage cycle

To understand how E-cadherin mediated cell-cell contacts are selectively destabilized in central but not marginal deep cells, we analysed cell-cell contact dynamics in the context of other cellular processes occurring at the same time. Cell-cell contact disassembly in the blastoderm centre (from high stage until the onset of doming) coincides with the last rounds of meta-synchronous cleavages within the blastoderm (cell cycle 11 to 13) [27,28]. Cleavages were associated with mitotic rounding of the dividing cells, reducing cell-cell contact size at metaphase (**Fig. 4a, b**; **Supplementary Fig. 4a** and **Supplementary Video 7**) likely due to the elevated interfacial tension at the cell-cell contact [29,30]. Interestingly, during the last cleavage cycles mitotic rounding-associated contact disassembly became increasingly more pronounced in central compared to marginal deep cells, although the extent of mitotic rounding in marginal cells was indistinguishable from central cells (**Fig. 4a, b; Supplementary Fig. 4a, b** and **Supplementary Video 7**). Furthermore, central deep cells failed to reassemble their contacts, while marginal cells typically rebuilt them to the initial size before disassembly (**Fig. 4b**, and **Supplementary Fig. 4c**). This combination of enhanced contact disassembly and reduced contact reassembly in central but not marginal deep cells ultimately led to central cells progressively losing their contacts. Collectively, these findings point to the possibility that successive rounds of cell cleavages trigger progressive central cell-cell contact loss, thereby setting the time of central blastoderm fluidization at the onset of doming.

To directly test this possibility, we sought to inhibit deep cell cleavages by keeping deep cells in interphase at pre-fluidization stages and evaluate how this would affect deep cell

cohesion and tissue viscosity during doming. To interfere with the last rounds of deep cell cleavages, we treated embryos at high stage with the S-phase inhibitor Hydroxyurea-Aphidicolin (HUA). HUA-treated deep cells failed to undergo their last three rounds of cleavages and associated mitotic rounding, preventing central deep cells from disassembling their cell-cell contacts, and the central blastoderm from fluidizing at the onset of doming (**Fig. 4a, c; Supplementary Fig. 4a, d** and **Supplementary Video 8**). In order to assess the functional relevance of this cleavage-dependent failure in cell-cell contact disassembly specifically within the deep cell layer, we transplanted HUA-treated central donor cells, which were stalled in the 10^{th} cell cycle, into the central blastoderm of untreated host embryos that had completed all their cleavage cycles by the onset of doming. At the time of transplantation, HUA-treated deep cells displayed a more cohesive and compact cell cluster compared to the neighbouring untreated host tissue (**Supplementary Fig. 4e**). This local change of cell cohesion by the transplanted cells was followed by reduced blastoderm thinning in the transplanted area (**Fig. 4d, e** and **Supplementary Video 9**). Notably, the transplanted donor cells in the host environment free of HUA eventually restarted cleaving and gradually disassembled their contacts at 50% epiboly, a stage where deep cell tissue cohesion/viscosity in the host embryo had already increased again (**Fig. 4b, Supplementary Fig. 4b, c** and **e**). Together, these findings indicate that the final rounds of deep cell cleavages are required for the initiation of doming by triggering central deep cell contact loss and thus blastoderm fluidization.

To determine whether mitotic rounding is responsible for deep cells in the blastoderm centre losing their contacts as previously suggested for other cells [31], we sought to reduce mitotic rounding without affecting cell cycle progression. To this end, we interfered with the

function of ERM proteins required for mitotic cell rounding by overexpressing dominant negative (DN) Ezrin [32–34]. Remarkably, DN Ezrin expressing central deep cells not only displayed impaired mitotic rounding, but also exhibited reduced cleavage-dependent contact disassembly, leading to larger and more stable contacts by the onset of doming than found in WT cells (**Fig. 4a-c** and **Supplementary Fig. 4a-c**). This suggests that mitotic rounding leads to contact loss between central deep cells. To directly address how impaired mitotic rounding-associated contact loss affects doming movements, we transplanted DN Ezrin expressing central deep cells into the centre of a WT control embryo. We found that transplanted DN Ezrin expressing donor tissue failed to undergo tissue fluidization and, consequently, inhibited central blastoderm thinning around the transplanted area during doming (**Fig. 4d, e; Supplementary Fig. 4f**). Together, these findings suggest that mitotic rounding of deep cells undergoing their final cleavage rounds is required for the initiation of doming by driving central deep cell contact loss and thus blastoderm fluidization.

Wnt11/Fz7-signaling determines the spatial pattern of blastoderm fluidization

Our observation that during cleavage cycle 12 and 13, central but not marginal cells exhibit mitotic rounding-dependent tissue fluidization (**Fig. 4b** and **Supplementary Fig. 4b, c**), suggests that a reinforcement mechanism might exist within the blastoderm margin that provides mechanical resistance against cleavage-mediated contact loss. Interestingly, during the last cleavage cycles several genes are expressed within the blastoderm margin, including the non-canonical Wnt signal *wnt11* [35] (**Fig. 5a**) and its receptor *fz7* [36], two genes previously implicated in regulating cell cohesion during zebrafish embryogenesis [36–38]. We thus reasoned that non-canonical Wnt signalling might be involved in suppressing mitotic rounding-induced contact loss within the blastoderm margin and thus spatially restricting

fluidization. To address this possibility, we analysed marginal blastoderm viscosity in *slb/wnt11* mutant embryos [37]. Strikingly, we found that at the onset of doming, not only central but also marginal deep cells from *slb* mutants progressively disassembled their contacts leading to ectopic marginal tissue fluidization (**Fig. 5b-e; Supplementary Fig. 5a-d** and **Supplementary Video 10**). Moreover, *slb* embryos displayed reduced blastoderm thinning (**Fig. 5f**), consistent with the predictions from our doming simulations in embryos with uniform low viscosity (**Fig. 1h**). Similar ectopic contact disassembly and tissue fluidization was observed within the blastoderm margin of mutants for the Wnt11 receptor Fz7 (MZ*fz7a/b*) (**Supplementary Fig. 5b-e**), suggesting that Wnt11 signals through its receptor Fz7 to provide mechanical resistance against cleavage-mediated contact loss in the margin. To address if in the absence of Wnt11/Fz7 signalling marginal cells would behave like central cells, we transplanted *slb* and MZ*fz7a/b* marginal cells into the central blastoderm of WT embryos. We found that - contrary to the situation when WT marginal deep cells were used as donor cells - transplanted mutant marginal cells allowed central blastoderm thinning to proceed normally by undergoing cell-cell contact loss indistinguishable from the surrounding WT central blastoderm (**Fig. 6a, b, e, g; Supplementary Fig. 5f-i**).

Interestingly, transplanted Wnt11-expressing marginal donor cells failed to influence cell cohesion in the neighbouring host central tissue (**Supplementary Fig. 6a**), suggesting that central cells might not be competent to respond to Wnt11. To address this possibility, we performed central-to-marginal deep cell transplantation experiments (**Supplementary Fig. 6b**). Central cells transplanted into the margin displayed contact loss and ectopic fluidization, resulting in local shape changes of the BYI at dome stage (**Supplementary Fig.**

289 **6c-f**). This suggests that central cells are unresponsive to Wnt11 signals within the
290 blastoderm margin that prevents the cleavage-mediated tissue fluidization. Next, we asked
291 whether central cells are unresponsive to Wnt11-signaling because they fail to express the
292 Wnt11 receptor Fz7a [36]. To address this possibility, we ectopically expressed Fz7a in central
293 cells and transplanted them into the blastoderm margin of either WT or *slb/wnt11* mutant
294 embryos (**Supplementary Fig. 6b**). Central donor cells expressing Fz7a acquired the
295 morphogenetic properties of their surrounding host tissue when transplanted into the
296 blastoderm margin of WT embryos, while they retained their original properties when
297 transplanted into the blastoderm margin of *slb* embryos (**Supplementary Fig. 6c-f**). This
298 suggests that central deep cells are unresponsive to Wnt11 because they fail to express
299 Fz7a.
300
301 **Wnt11/Fz7-signaling promotes marginal deep cell cohesion by enhancing actomyosin**
302 **contractility**
303 Non-canonical Wnt-signalling has previously shown to promote both actomyosin
304 contractility and cell cohesion [36,38,39]. We therefore speculated that Wnt11/Fz7-signaling
305 promotes deep cell cohesion and thus prevent cleavage-mediated tissue fluidization in the
306 marginal blastoderm by enhancing actomyosin contractility. To test this possibility, we first
307 asked whether marginal deep cells with active Wnt11/Fz7-signaling are more contractile
308 than central cells. For analysing cell contractility, we performed marginal-to-central
309 transplantation experiments and analysed interfacial tensions to the surrounding interstitial
310 fluid as readout of cortical actomyosin contractility using 3D-VFM [40]. This analysis showed
311 that WT marginal cells displayed higher cortical tension than central cells (**Fig. 6f**). In
312 contrast, when performing marginal-to-central transplantations using *slb* mutant cells no

such increased cortical tension was detectable (**Fig. 6f**). Together, this suggests that Wnt11/Fz7 increases cortical tension in marginal deep cells that might account for their ability to resist cleavage-mediated contact disassembly and thus tissue fluidization (**Fig. 6c-g**). Further support for this notion came also from our observation that the localization of Actin and E-cadherin to cell-cell contact edges, previously shown to depend on cortical tension [26], was found in marginal deep cells from WT but not *slb* mutant embryos (**Fig. 6h**).

To directly test whether Wnt11/Fz7 signalling promotes marginal deep cell contact stability by up-regulating cortical tension, we increased cortical tension in *slb* mutant marginal cells by overexpressing CA RhoA and transplanted those cells into the blastoderm centre of WT embryos. Strikingly, transplanted *slb* marginal deep cells overexpressing CA RhoA – similar to WT marginal cells – not only displayed increased cortical contractility and contact stability but also failed to undergo tissue fluidization, leading to reduced blastoderm thinning around the transplanted cells (**Fig. 6a-g**). Moreover, *slb* marginal cells overexpressing CA RhoA showed enhanced localization of Actin and E-cadherin to their cell-cell contact edges, typically found in WT marginal cells forming stable contacts (**Fig. 6h**). Collectively, these results indicate that non-canonical Wnt signalling maintains marginal tissue integrity by upregulating actomyosin contractility, thereby promoting cell-cell contact stability and preventing cleavage-mediated contact loss and tissue fluidization.

DISCUSSION

Tissue material properties, such as viscoelasticity, can vary within embryonic tissues, and regulated changes in tissue viscoelasticity have been proposed to affect tissue morphogenesis in development [5,7,10]. Our findings by both measuring and manipulating

tissue viscosity/fluidity, provide direct functional evidence for an important role of this process in embryo morphogenesis. Importantly, tissue viscosity and TST have previously been proposed to be co-regulated in development [10]. Our observation, however, that in none of our experimental approaches to modulate tissue viscosity, except the overexpression of CA RhoA, TST (as determined by 3D-VFM [40]) was recognizably changed (**Supplementary Note** and **Supplementary Table 2**), suggests that blastoderm viscosity can be regulated independently from TST. It further shows that the effects on doming movements observed after changing blastoderm viscosity were due to changes in tissue viscosity and not TST.

A key finding of our study is that blastoderm fluidization is temporally controlled by the last rounds of meta-synchronous cell cleavages, thereby identifying an unexpected morphogenetic function of synchronized cell cleavages in modulating tissue fluidity. Previous studies in chick gastrulation have shown that cell divisions promote cellular rearrangements within the epiblast [41], pointing at the possibility that cell divisions might also function in this process by modulating tissue fluidity. Moreover, theoretical studies on the role of cell divisions within epithelial cell layers have predicted that the relaxation time of an elastic solid tissue is set by the rate of cell divisions [11], suggesting that cell divisions not only can trigger a tissue fluidization on short time-scales by inducing contact disassembly, as shown in our study, but also can act on longer time scales to relax tissue stress. Finally, our observation that only after completion of the last cell cleavage cycle, blastoderm cells begin to undergo active radial cell intercalations (**Supplementary Fig. 1b**), suggests that cell divisions can also influence tissue morphogenesis by suppressing active cell movements.

Our finding of Wnt11/Fz7-signaling spatially restricting the effect of cell cleavages on tissue fluidization to the blastoderm centre by promoting cell cohesion within the blastoderm margin (**Fig. 7**), is consistent with previous findings of non-canonical Wnt signalling promoting cell cohesion in both vertebrate and invertebrate embryogenesis. In mouse embryos, for instance, non-canonical Wnt9a-signaling has been suggested to influence the final sorting of the inner cell mass by regulating cell cohesion [42,43], while in the zebrafish embryos, non-canonical Wnt11 signalling is thought to promote collective migration of prechordal plate progenitors by regulating E-cadherin mediated adhesion between these cells [38,44]. How these effects on cell cohesion translate in changes of tissue material properties is yet unknown, but it is intriguing to speculate that non-canonical Wnt signalling displays a conserved function in early embryo morphogenesis by regulating cell cohesion and, consequently, tissue viscosity/fluidity.

Finally, although previous observations suggested that cell cohesion linearly correlates with tissue viscosity [10], our data suggest that in the zebrafish blastoderm, gradual and small reduction in cell cohesion leads to a sharp drop in tissue viscosity (**Fig. 7**). Such abrupt changes in tissue rheology resemble phase transitions, where a system can change its phase upon small changes in a system parameter [14,45]. This points to the intriguing possibility that tissue phase transitions triggered by small changes in cell cohesion might represent a general regulatory mechanism by which tissues undergo large scale shape changes.

ACKNOWLEDGEMENTS

We thank Otger Campas and members of the Heisenberg laboratory for technical advice and discussions, and the Bioimaging and zebrafish facilities of the IST Austria for continuous

support. This work was supported by a postdoctoral fellowship from EMBO Long-term fellowships to N.I.P (ALTF-534 2016) and an ERC Advanced Grant (MECSPEC) to C.-P.H. S.G. and G.S. were supported by The Francis Crick Institute, which receives its core funding from Cancer Research UK (FC001317), the UK Medical Research Council (FC001317) and the Wellcome Trust (FC001317).

AUTHOR CONTRIBUTIONS

N.I.P and C.-P.H. designed the research. N.I.P. performed the experiments and analysed the experimental data. G.S. and S.G. developed the theoretical doming models. S.G. performed the doming simulations. E.H. analysed cell cohesion and tissue rigidity data. N.I.P and C.-P.H. wrote the manuscript.

The authors have no financial and non-financial competing interests.

REFERENCES

1. Heisenberg, C. P. & Bellaïche, Y. Forces in tissue morphogenesis and patterning. *Cell* **153,** (2013).
2. Petridou, N. I., Spiró, Z. & Heisenberg, C. P. Multiscale force sensing in development. *Nat. Cell Biol.* **19,** 581–588 (2017).
3. Gonzalez-Rodriguez, D., Guevorkian, K., Douezan, S. & Brochard-Wyart, F. Soft Matter Models of Developing Tissues and Tumors. *Science (80-.).* **338,** 910 LP-917 (2012).
4. Forgacs, G., Foty, R. A., Shafrir, Y. & Steinberg, M. S. Viscoelastic properties of living embryonic tissues: A quantitative study. *Biophys. J.* **74,** 2227–2234 (1998).

5. Lawton, A. K. *et al.* Regulated tissue fluidity steers zebrafish body elongation. *Development* **140,** 573–582 (2013).

6. Mongera, A. *et al.* A fluid-to-solid jamming transition underlies vertebrate body axis elongation. *Nature* (2018). doi:10.1038/s41586-018-0479-2

7. Serwane, F. *et al.* In vivo quantification of spatially varying mechanical properties in developing tissues. *Nat. Methods* **14,** 181–186 (2017).

8. Moore, S. W., Keller, R. E. & Koehl, M. A. The dorsal involuting marginal zone stiffens anisotropically during its convergent extension in the gastrula of Xenopus laevis. *Development* **121,** 3131 LP-3140 (1995).

9. Shook, D. R., Kasprowicz, E. M., Davidson, L. A. & Keller, R. Large, long range tensile forces drive convergence during Xenopus blastopore closure and body axis elongation. *Elife* **7,** e26944 (2018).

10. David, R. *et al.* Tissue cohesion and the mechanics of cell rearrangement. *Development* **141,** 3672–3682 (2014).

11. Ranft, J. *et al.* Fluidization of tissues by cell division and apoptosis. *Proc. Natl. Acad. Sci.* **107,** 20863–20868 (2010).

12. Stirbat, T. V. *et al.* Fine Tuning of Tissues' Viscosity and Surface Tension through Contractility Suggests a New Role for α-Catenin. *PLoS One* **8,** (2013).

13. Bi, D., Lopez, J. H., Schwarz, J. M. & Manning, M. L. A density-independent rigidity transition in biological tissues. *Nat. Phys.* **11,** 1074–1079 (2015).

14. Bi, D., Yang, X., Marchetti, M. C. & Manning, M. L. Motility-driven glass and jamming transitions in biological tissues. *Phys. Rev. X* **6,** 1–13 (2016).

15. Angelini, T. E. *et al.* Glass-like dynamics of collective cell migration. *Proc. Natl. Acad. Sci.* **108,** 4714–4719 (2011).

16. Sadati, M., Taheri Qazvini, N., Krishnan, R., Park, C. Y. & Fredberg, J. J. Collective migration and cell jamming. *Differentiation* **86,** 121–125 (2013).

17. Bruce, A. E. E. Zebrafish epiboly: Spreading thin over the yolk. *Dev. Dyn.* **245,** 244–258 (2016).

18. Lepage, S. E. & Bruce, A. E. E. Zebrafish epiboly: Mechanics and mechanisms. *Int. J. Dev. Biol.* **54,** 1213–1228 (2010).

19. Morita, H. *et al.* The Physical Basis of Coordinated Tissue Spreading in Zebrafish Gastrulation. *Dev. Cell* **40,** 354–366.e4 (2017).

20. Davidson, L. A. *Embryo Mechanics. Balancing Force Production with Elastic Resistance During Morphogenesis*. *Current Topics in Developmental Biology* **95,** (Elsevier Inc., 2011).

21. Guevorkian, K., Colbert, M. J., Durth, M., Dufour, S. & Brochard-Wyart, F. Aspiration of biological viscoelastic drops. *Phys. Rev. Lett.* **104,** 1–4 (2010).

22. Guevorkian, K. & Maître, J. L. Micropipette aspiration: A unique tool for exploring cell and tissue mechanics in vivo. *Methods Cell Biol.* **139,** 187–201 (2017).

23. Fukazawa, C. *et al.* poky/chuk/ikk1 is required for differentiation of the zebrafish embryonic epidermis. *October* **346,** 272–283 (2011).

24. Song, S. *et al.* Pou5f1-Dependent EGF Expression Controls E-Cadherin Endocytosis, Cell Adhesion, and Zebrafish Epiboly Movements. *Dev. Cell* **24,** 486–507 (2013).

25. Shimizu, T. *et al.* E-cadherin is required for gastrulation cell movements in zebrafish. *Mech. Dev.* **122,** 747–763 (2005).

26. Maitre, J.-L. *et al.* Adhesion Functions in Cell Sorting by Mechanically Coupling the Cortices of Adhering Cells. *Science (80-.).* **338,** 253–256 (2012).

27. Mendieta-Serrano, M. A., Schnabel, D., Lomelí, H. & Salas-Vidal, E. Cell Proliferation

457 Patterns in Early Zebrafish Development. *Anat. Rec.* **296,** 759–773 (2013).
458 28. Kimmel, C. B., Ballard, W. W., Kimmel, S. R., Ullmann, B. & Schilling, T. F. Stages of
459 embryonic development of the zebrafish. *Dev. Dyn. an Off. public* **203,** 253–310
460 (1995).
461 29. Sorce, B. *et al.* Mitotic cells contract actomyosin cortex and generate pressure to
462 round against or escape epithelial confinement. *Nat. Commun.* **6,** (2015).
463 30. Stewart, M. P. *et al.* Hydrostatic pressure and the actomyosin cortex drive mitotic cell
464 rounding. *Nature* **469,** 226–231 (2011).
465 31. Théry, M. & Bornens, M. Get round and stiff for mitosis. *HFSP J.* **2,** 65–71 (2008).
466 32. Rosenblatt, J. Mitosis: Moesin and the Importance of Being Round. *Curr. Biol.* **18,** 1–6
467 (2015).
468 33. Carreno, S. *et al.* Moesin and its activating kinase Slik are required for cortical stability
469 and microtubule organization in mitotic cells. *J. Cell Biol.* **180,** 739–746 (2008).
470 34. Tachibana, K., Haghparast, S. M. A. & Miyake, J. Inhibition of cell adhesion by
471 phosphorylated Ezrin/Radixin/Moesin. *Cell Adhes. Migr.* **9,** 502–512 (2015).
472 35. Makita, R., Mizuno, T., Koshida, S., Kuroiwa, A. & Takeda, H. Zebrafish wnt11: Pattern
473 and regulation of the expression by the yolk cell and No tail activity. *Mech. Dev.* **71,**
474 165–176 (1998).
475 36. Witzel, S., Zimyanin, V., Carreira-Barbosa, F., Tada, M. & Heisenberg, C. P. Wnt11
476 controls cell contact persistence by local accumulation of Frizzled 7 at the plasma
477 membrane. *J. Cell Biol.* **175,** 791–802 (2006).
478 37. Heisenberg, C.-P. *et al.* Silberblick / Wnt11 mediates convergent extension
479 movements during zebrafish gastrulation. *Nature* **405,** 76–81 (2000).
480 38. Ulrich, F. *et al.* Slb/Wnt11 controls hypoblast cell migration and morphogenesis at the

onset of zebrafish gastrulation. *Development* **130,** 5375 LP-5384 (2003).

39. Dzamba, B. J., Jakab, K. R., Marsden, M., Schwartz, M. A. & DeSimone, D. W. Cadherin Adhesion, Tissue Tension, and Noncanonical Wnt Signaling Regulate Fibronectin Matrix Organization. *Dev. Cell* **16,** 421–432 (2009).

40. Brodland, G. W. *et al.* CellFIT: A Cellular Force-Inference Toolkit Using Curvilinear Cell Boundaries. *PLoS One* **9,** e99116 (2014).

41. Firmino, J., Rocancourt, D., Saadaoui, M., Moreau, C. & Gros, J. Cell Division Drives Epithelial Cell Rearrangements during Gastrulation in Chick. *Dev. Cell* **36,** 249–261 (2016).

42. Meilhac, S. M. *et al.* Active cell movements coupled to positional induction are involved in lineage segregation in the mouse blastocyst. *Dev. Biol.* **331,** 210–221 (2009).

43. Xenopoulos, P., Kang, M. & Hadjantonakis, A.-K. Cell Lineage Allocation Within the Inner Cell Mass of the Mouse Blastocyst. *Results Probl. Cell Differ.* **55,** 185–202 (2012).

44. Ulrich, F. *et al.* Wnt11 functions in gastrulation by controlling cell cohesion through Rab5c and E-Cadherin. *Dev. Cell* **9,** 555–564 (2005).

45. Schoetz, E.-M., Lanio, M., Talbot, J. A. & Manning, M. L. Glassy dynamics in three-dimensional embryonic tissues. (2013). doi:10.1098/rsif.2013.0726

46. Detrich, W. H. I., Westerfield, M. & Zon, L. I. *The zebrafish: Biology*. *Methods in cell biology* (1999).

47. Behrndt, M. *et al.* Forces Driving Epithelial Spreading in Zebrafish Gastrulation. *Science (80-.).* **338,** 257 LP-260 (2012).

48. Quesada-Hernández, E. *et al.* Stereotypical cell division orientation controls neural

505 rod midline formation in zebrafish. *Curr. Biol.* **20,** 1966–1972 (2010).
506 49. Wagner, D. S., Dosch, R., Mintzer, K. A., Wiemelt, A. P. & Mullins, M. C. Maternal
507 Control of Development at the Midblastula Transition and beyond: Mutants from the
508 Zebrafish II. *Dev. Cell* **6,** 781–790 (2004).
509 50. Kimmel, C. B. & Law, R. D. Cell lineage of zebrafish blastomeres. I. Cleavage pattern
510 and cytoplasmic bridges between cells. *Dev. Biol.* **108,** 78–85 (1985).
511 51. Kimmel, R. A. & Meyer, D. *Molecular regulation of pancreas development in zebrafish*.
512 *Methods in Cell Biology* **100,** (Elsevier Inc., 2010).
513 52. Iioka, H., Ueno, N. & Kinoshita, N. Essential role of MARCKS in cortical actin dynamics
514 during gastrulation movements. *J. Cell Biol.* **164,** 169–174 (2004).
515 53. Arboleda-Estudillo, Y. *et al.* Movement Directionality in Collective Migration of Germ
516 Layer Progenitors. *Curr. Biol.* **20,** 161–169 (2010).
517 54. Keller, P. J., Schmidt, A. D., Wittbrodt, J. & Stelzer, E. H. K. Reconstruction of Zebrafish
518 Early Embryonic Development by Scanned Light Sheet Microscopy. *Science (80-.).*
519 **322,** 1065 LP-1069 (2008).
520 55. Ruprecht, V. *et al.* Cortical contractility triggers a stochastic switch to fast amoeboid
521 cell motility. *Cell* **160,** 673–685 (2015).
522 56. Jopling, C. & den Hertog, J. Fyn/Yes and non-canonical Wnt signalling converge on
523 RhoA in vertebrate gastrulation cell movements. *EMBO Rep.* **6,** 426–431 (2005).
524 57. Krens, S. F. G. *et al.* Interstitial fluid osmolarity modulates the action of differential
525 tissue surface tension in progenitor cell segregation during gastrulation. *Development*
526 **144,** 1798–1806 (2017).
527 58. Brodland, G. W. *et al.* Video force microscopy reveals the mechanics of ventral furrow
528 invagination in Drosophila. *Proc. Natl. Acad. Sci.* **107,** 22111 LP-22116 (2010).

Figure legends

Figure 1

Changes in tissue fluidity correlate spatiotemporally with changes in tissue deformation.

a, Schematic representation of a sagittal section of a zebrafish embryo at the onset of doming defining marginal and central blastoderm regions. **b,** Bright-field single plane images of an exemplary zebrafish embryo before (high, sphere), during (onset, dome) and after doming (50% epiboly). **c,** Schematic diagram and plot of EVL spreading as a function of time (n=8 embryos, N=3). **d,** Schematic diagram of blastoderm-to-yolk interface (BYI) displacement in central (red) versus marginal (green) blastoderm and plot as a function of time (n=6 embryos, N=3). **e,** Schematic diagram and plot of the relative central blastoderm height (red arrow) as a function of time (n=4 embryos, N=2). **f,** Bright-field images of exemplary deep cell aspirations in the blastoderm centre and margin of intact embryos, and in central blastoderm explants at the onset of doming. Black arrowheads indicate how far the cells have flown into the micropipette under the same pressure. Bar plot of blastoderm viscosity calculated from the aspiration experiments (n=83 embryos, N=9 for centre; n=81 embryos, N=9 for margin; n=37 explants, N=3 for explants). **g,** Shape changes of a 3-rectangle system representing the deep cell tissue as a passive fluid with equal or patterned viscosity (lower in the centre) and subjected to an external constant force by the expanding EVL (black rectangle). **h,** Comparison of experimentally measured (pale red) and simulated (dark red) relative blastoderm height as a function of time for deep cell layer with high uniform viscosity (chi-squared R=0.116), low uniform viscosity (chi-squared R=0.064) and patterned viscosity (90% reduction in the blastoderm centre; chi-squared R=0.032), in the presence of surface tissue tension reduction. Experimental data (blastoderm height and

central blastoderm viscosity) are taken from (e, f). Simulation parameters are reported in Supplementary Table 1 and are obtained from Morita et al [19]. Top panels show simulated embryo shapes at 30 min of doming.

In all plots, the onset of doming is indicated with grey dashed line. Data are mean ± s.e.m. N is the number of independent embryo batches; Kruskal-Wallis test. Scale bars: (b, f) 100 µm.

Figure 2

Spatiotemporally patterned blastoderm fluidization is required for doming.

a, Schematic illustration of homotypic (centre to centre at high stage), heterotypic (margin to centre at high stage) and heterochronic (high stage centre to sphere stage centre) deep cell transplantations. **b,** Exemplary single plane fluorescence/bright-field images of the transplanted embryos described in (a), at the onset and end of doming. Transplanted cells are fluorescently marked by H2B-GFP pseudo-coloured in red, green and cyan, respectively. **c,** BYI displacement in the blastoderm centre containing the transplanted cells versus the margin free of transplanted cells as a function of time during doming (homotypic n=7 transplants; heterotypic n=8 transplants; heterochronic n=5 transplants; N=3). **d,** Bright-field/fluorescent images of exemplary deep cell aspirations in the transplantation experiments described in (a). Black arrowheads indicate how far the cells have flown into the micropipette under the same pressure. Bar plot on the right shows tissue viscosity calculated from the deep cell aspiration experiments in the transplanted area at the onset of doming (homotypic n=5; heterotypic n=8; heterochronic n=5; N=4).

The onset of doming is indicated with grey dashed line. Data are mean ± s.e.m. N is the number of independent embryo batches; Kruskal-Wallis test. Scale bars: (b, d) 100 µm.

Figure 3

De-stabilization of E-cadherin contacts coincides with tissue fluidity changes.

a, Exemplary high-resolution images of central and marginal deep cells at high and onset of doming stages. Interstitial fluid accumulations (yellow arrowheads) are marked by dextran (cyan), nuclei by H2B-GFP (blue) and membranes by membrane-RFP (centre, red; margin, green). **b,** Bar plot of cell-cell contact time normalized to the total duration of the indicated stages (centre n=80; margin n=80; N=3). **c,** Plot of cell-cell contact length normalized to cell diameter during doming (for each time point: centre n=15; margin n=15; N=3). **d,** Plot of the number of cell-cell contacts per cell during doming (centre n=1,340; margin n=1,073; N=3). **e**, Exemplary confocal images of transplanted donor and host deep cells within the blastoderm centre in the experiments shown in Fig. 2a at the onset of doming. Donor cells are marked by membrane-GFP (homotypic, red; heterotypic, green; heterochronic, cyan), host cells by membrane-RFP (grey), and interstitial fluid by dextran (blue). **f,** Plot of normalized cell-cell contact length between donor cells during doming (for each time point: homotypic cells n=8; heterotypic cells n=9; heterochronic cells n=10; N=3). **g,** Bar plot of normalized cell-cell contact time between donor cells (homotypic cells n=280; heterotypic cells n=215; heterochronic cells n=144; N=3). At the x-axis, the developmental stage of the host is written in black, and of the heterochronic donor in cyan. **h,** Exemplary high-resolution images of deep cell-cell contacts in the blastoderm centre versus margin at high stage and onset of doming stained for E-cadherin (grey) and phalloidin/Actin (magenta). Optical sections at the level of the contact (left images), and cross-sections of the contact (right images) outlined by the dashed box. Intensity profiles show the average distribution of E-cadherin and Actin across the diameter of the contact (centre high n=7 contacts;

600 margin high n=4 contacts; centre onset n=6 contacts; margin onset n=6 contacts; N=2). Red
601 stars indicate contact edges.
602 In all plots the grey dashed line indicates the onset of doming. Data are mean ± s.e.m. N is
603 the number of embryos; Kruskal-Wallis test. Scale bars: (a, e, h) 20 µm; (h cross sections) 10
604 µm.
605
606 **Figure 4**
607 **Deep cell cleavage cycle sets the time of central blastoderm fluidization.**
608 **a,** Confocal images of WT central, WT marginal, HUA-treated central and DN Ezrin
609 expressing central deep cells. Plasma membrane is labelled by membrane-RFP pseudo-
610 coloured in red, green, yellow and magenta, respectively, nuclei by H2B-GFP in blue, and
611 interstitial fluid by dextran in cyan. White arrowheads indicate deep cell-cell contacts. **b,**
612 Deep cell-cell contact length normalized to cell diameter plotted at the following time
613 points: 9 min before metaphase (t_{bm}), at metaphase (t_m) and 9 min after metaphase (t_{am}) for
614 cycles 11^{th} to 13^{th} for WT central, WT marginal, DN Ezrin expressing central deep cells and
615 HUA-treated and transplanted central donor deep cells (WT centre n=26 contacts; WT
616 margin n=16 contacts; HUA-treated and transplanted centre n=10 contacts; DN Ezrin centre
617 n=20 contacts; N=3). Dashed lines indicate metaphase (grey for WT central, WT marginal
618 and DN Ezrin central cells; yellow for HUA-treated and transplanted central cells). Cyan
619 shaded box outlines the period of contact disassembly. Orange shaded box outlines the
620 period of contact re-assembly. **c**, Bar plot of the deep cell-cell contact time normalized to
621 the total duration of the indicated stages for the different conditions outlined in (a) (WT
622 centre n=80; WT margin n=80; HUA centre n=160; DN Ezrin centre n=120; N=4). **d**,
623 Exemplary single plane fluorescence/bright-field images of transplanted embryos containing

WT, HUA-treated and DN Ezrin expressing donor central cells in the central WT host blastoderm at the onset and end of doming. Transplanted cells are fluorescently marked by H2B-GFP in red, yellow and magenta, respectively**. e**, BYI displacement as a function of time during doming for the transplanted embryos shown in (d) (WT n=10 transplants; HUA n=6 transplants; DN Ezrin n=4 transplants; N=3).

The onset of doming is indicated with grey dashed line. Data are mean ± s.e.m. N is the number of embryos (in b, c) and number of independent embryo batches (in e); Kruskal-Wallis test. Scale bars: (a) 20 μm; (d) 100 μm.

Figure 5

Wnt11-signalling suppresses marginal blastoderm fluidization.

a, Exemplary animal and side views of *wnt11* expression (white arrowheads) in zebrafish embryos at the onset of doming. **b,** Bar plot of cell-cell contact time normalized to the total duration of the indicated stages (WT margin n=80; *slb* margin n=75; N=3). **c,** Plot of cell-cell contact length normalized to cell diameter during doming (for each time point: WT margin n=20; *slb* margin n=20; N=3). **d,** Plot of the number of cell-cell contacts per cell during doming (WT margin n=1,073; *slb* margin n=827; N=3). **e,** Bright-field images of exemplary deep cell aspirations in the blastoderm centre and margin of *slb* mutant embryos. Black arrowheads indicate how far the cells have flown into the aspiration pipette under the same pressure. Bar plot on the right shows blastoderm viscosity calculated from the aspiration experiments for the indicated stages (WT centre sphere n=4; WT margin sphere n=3; WT centre onset n=8; WT margin onset n=18; *slb* centre sphere n=6; *slb* margin sphere n=10; *slb* centre onset n=4; *slb* margin onset n=12; N=3). **f,** Bright-field images of representative WT

and *slb* embryos at dome stage. Plot on the right shows relative blastoderm height as a function of time (WT n=4 embryos; *slb* n=7 embryos; N=4).

The onset of doming is indicated with grey dashed line. Data are mean ± s.e.m. N is the number of embryos (in b-d) and number of independent embryo batches (in e, f); Kruskal-Wallis test. Scale bars: (a) 20 µm; (e, f) 100 µm.

Figure 6

Wnt11-signalling prevents marginal blastoderm tissue fluidization by promoting cortical-tension dependent cell cohesion.

a, Exemplary single plane fluorescence/bright-field images of WT embryos with WT (green), *slb* (yellow) and *slb*+CARhoA (cyan) marginal cells (marked by H2B-GFP) transplanted into the blastoderm centre. **b,** BYI displacement as a function of time for the conditions in (a) (WT n=4; *slb* n=6; *slb*+CARhoA n=5; N=3). **c, d,** Bright-field/fluorescent images of exemplary aspirations of transplanted deep cells (c) and corresponding tissue viscosities (d) for the conditions in (a) at the onset of doming (WT n=8; *slb* n=10; *slb*+CARhoA n=7; N=3). Black arrowheads (c) indicate how far the cells have flown into the micropipette under the same pressure. **e,** Exemplary confocal images of the conditions in (a). Donor cells are marked by membrane-GFP (WT, green; *slb*, yellow; *slb*+CARhoA, cyan), host cells by membrane-RFP (grey), nuclei by H2B-GFP (yellow and cyan in *slb* and *slb*+CARhoA cells, respectively) and interstitial fluid by dextran (blue). **f,** Bar plot of the ratio of relative cell-medium interfacial tensions (γ_{cm}) of donor cells to that of host cells for the transplants in (e) (WT margin transplants: N=6; *slb* margin transplants: N=8; *slb*+CARhoA margin transplants: N=8). **g,** Bar plot of normalized cell-cell contact time between transplanted cells for the conditions in (e) (WT n=240; *slb* n=160; *slb*+CARhoA n=200; N=4). **h**, Exemplary high-resolution images of

deep cell-cell contacts, stained for E-cadherin (grey) and phalloidin/Actin (magenta) in the margin of WT, *slb* and *slb*+CARhoA embryos at the onset doming. Optical sections at the level of the contact (left images) and cross-sections of the contact (right images) outlined by the dashed box in the left image. Intensity profiles show the distribution of E-cadherin and Actin across the contact (WT n=14 contacts; *slb* n=7 contacts; *slb*+CARhoA n=11; N=2). Red asterisks indicate contact edges.

In all plots, the grey dashed line indicates the doming onset. Data are mean ± s.e.m. N is the number of embryos (in f-h) and number of independent embryo batches (in b, d); Kruskal-Wallis test. Scale bars: (a, c) 100 µm; (e) 20 µm; (h) 10 µm; (h, cross sections) 5 µm.

Figure 7

Combinatorial activities of cell cleavages and morphogen signalling define a critical point of cell connectivity triggering blastoderm fluidization.

Schematic diagram of the mechanism defining the spatiotemporal pattern of blastoderm fluidization at the onset of zebrafish doming. Sequential cell cleavages associated with mitotic cell rounding lead to gradual deep cell-cell contact loss, which at a critical threshold level of cohesion (blue circle; expressed as a function of cell-cell contact time, number and size) results in blastoderm fluidization. Non-canonical Wnt signalling confines tissue fluidization to the blastoderm centre by stabilizing the deep cell-cell contacts in the margin, thereby preventing mitotic rounding mediated contact disassembly.

METHODS

Zebrafish handling

Zebrafish (*Danio rerio*) were maintained under a 14-h light/10-h dark cycle [46]. The following zebrafish strains were used in this study: wild type (WT) AB, *Tg(actb2:Lifeact-EGFP)* [47], *Tg(actb2:GFP-Has.UTRN)* [47], *slb* / MZ *wnt11* [37], MZ *fz7ab* (MZ *fzd7a* e3/ *fzd7b* hu2986) [48], *poky* (*pky*) [49]. Zebrafish embryos were grown at 25-28.5 ^{o}C in E3 embryo medium and staged as previously described [50]. For precise staging before and during doming, the last rounds of meta-synchronous cleavages and resulting changes in cell size were used as temporal hallmarks defining developmental time relative to the onset of doming. Embryonic manipulations of WT embryos were performed in 1x Danieau's solution [58 mM NaCl, 0.7 mM KCl, 0.4 mM $MgSO_4$, 0.6 mM $Ca(NO_3)_2$, 5 mM HEPES (pH 7.2)]. For experiments on *pky* embryos (Supplementary Fig. 3), 1x Danieau's solution was used as hypotonic medium (~120 mOsm/L), and 1x Ringer's [116 mM NaCl, 2.9 mM KCl, 1.8 mM $CaCl_2$, 5 mM HEPES (pH 7.2)] as isotonic medium (~258 mOsm/L).

Embryo microinjections

Zebrafish embryos were injected using glass capillary needles (30-0020, Harvard Apparatus, MA, USA), which were pulled by a needle puller (P-97, Sutter Instrument) and attached to a microinjector system (PV820, World Precision Instruments). Microinjections of mRNAs were performed at one-cell stage. mRNAs were synthesized using mMACHINE SP6 kit (Ambion). The following mRNAs were injected: 70 pg membrane GFP [51], 70 pg membrane RFP [52], 70 pg H2A mCherry [53], 70 pg H2B GFP [54], 250 pg DN Ezrin (T564A) [55], 100 pg Fz7a-Neon [36], 2 pg CA RhoA (RhoA V14) [56]. To label the interstitial fluid, 1 nl of 0.6 mg/ml dextran Alexa Fluor 647

(10,000 MW; D22914, Invitrogen) was injected in the blastoderm of 1k-stage embryos (~ 3 hpf).

Explants

Central blastoderm explants for micropipette aspirations were prepared in 1x Danieau's solution by dechorionating donor embryos with forceps and excising animal pole regions of the blastoderm (excluding the margin) with a hair-knife. Explants were left to round up for 30 min at 25^{o}C prior to aspiration.

Deep cell transplantations

Donor and host embryos were dechorionated with forceps and transferred into 1x Danieau's embryo medium. For all the transplantation conditions a bevelled fire-polished transplantation needle with a 45 µm inner diameter (Biomedical Instruments) attached to a syringe system was used. For the homotypic transplantations, approximately 3 nl of deep cells (~ 5% of the blastoderm volume) was removed either from the central or marginal region of the blastoderm of a high stage donor embryo and transplanted to the central or marginal region of the blastoderm of a high stage host embryo, respectively. For the heterotypic transplantations, approximately 3 nl of deep cells was removed either from the marginal or central region of the blastoderm of a high stage donor embryo and transplanted to the central or marginal region of the blastoderm of a high stage host embryo, respectively. For the heterochronic transplantations, approximately 3 nl of deep cells was removed from the central region of the blastoderm of a high stage donor embryo and transplanted to the central region of the blastoderm of a sphere stage host embryo. For the

beads transplantations, approximately 30 E-cadherin coated beads were transferred with a transplantation needle into the central blastoderm of high stage host embryos.

Isolation and *ex vivo* culture of deep cells

Deep cell isolation was performed in pre-warmed (25 ^{o}C) CO_2 independent DMEM/F-12 medium (11039-021, Sigma) as follows: for isolating central deep cells, the blastoderm of 1k-stage embryos was excised from the yolk cell, and the deep cell tissue in the blastoderm centre was shaved off the EVL using a hair-knife. For isolating marginal deep cells, the blastoderm of 1k-stage embryos was excised from the yolk cell, the remaining yolk was removed from marginal regions of the blastoderm, and deep cell tissue from the blastoderm margin was shaved off the EVL using a hair-knife. A mixture of either central or marginal deep cell tissues from 10 embryos was transferred with a serum-coated 10 µl micropipette into a 1.5 ml Eppendorf tube containing DMEM/F-12. Upon slight shaking, deep cells were dissociated and transferred onto glass coverslips passivated with 1% BSA and coated with 3% methylcellulose (M0387, Sigma).

Bead coating

For coating, Protein A-conjugated 4% agarose beads of an average diameter of 17 µm (customized product, ABT-Agarose Bead Technologies), were washed 2x in 1x PBS, then incubated with 50 µg/ml mouse E-cadherin/Fc chimera (E2153, Sigma) for 1 hour at RT, washed 3x in 1x PBS, incubated with 10 µg/ml of rabbit Alexa Fluor 546 anti-goat secondary antibody (A-21085, ThermoFisher Scientific) for 30 min at RT, washed 3x in 1x PBS and diluted in 10 µl of 1x Danieau's solution.

Block of cell division

Dechorionated embryos were treated with a cocktail of 60 mM hydroxyurea (H8627, Sigma) and 300 µM aphidicolin (A0781, Sigma) (HUA) from 1-k cell stage onwards.

Micropipette aspiration and viscosity / surface tension measurements

Blastoderm viscosity was measured by micropipette aspiration based on previously established protocols [18]. Briefly, embryos were placed on 3% methylcellulose coated glass coverslips in 1x Danieau's solution (or 1x Ringer's when stated) on an inverted Leica SP5 microscope. Fire-polished, passivated (with heat inactivated FBS) micropipette of 25, 35 and 45 µm inner diameter, 30^{o} bent, with a spike end (Biomedical Instruments) was inserted into the central or marginal blastoderm, just below the EVL. The micropipette movements were controlled by motorized micromanipulators (Eppendorf Transferman, Nk2). Upon insertion of the pipette in the blastoderm, aspiration pressure of 250, 200 or 150 Pa depending on the pipette size (**Supplementary Note**) was immediately applied using a Microfluidic Flow Control System Pump (Fluigent, Fluiwell) (with negative pressure ranging from 7-750 Pa, a pressure accuracy of 7 Pa and change rate of 200 Pa.s^{-1}) and the Dikeria micromanipulation software. Pressure was applied until the tissue flew into the pipette at a constant velocity (for ~5 min, except the cases where the tissue was fluidized and the deformation was too fast) and then pressure was immediately released. Images were acquired every 500 ms monitoring the aspiration and relaxation of the tissue. When aspirating transplants, only cases in which more than 50% of the aspirated tissue was consisting of transplanted cells, were taken into consideration for the viscosity measurements. During the aspiration no wound response was observed neither in the EVL nor in the aspirated deep cells (**Supplementary Note**). Yolk viscosity was measured using a

95 micropipette with 35 µm inner diameter, a 30^{o} bent and a spike, which was inserted in the
96 middle of the yolk at the onset of doming. EVL viscosity was measured using a micropipette
97 with 25 or 40 µm inner diameter, a 30^{o} bent, and a straight end, which was applied on the
98 surface of the EVL during doming. Viscosity calculations were performed as previously
99 described [21,22]. Briefly, the tongue length for each time point was measured using a
100 customized Fiji macro, and changes in tongue length during aspiration and relaxation were
101 then plotted over time (**Supplementary Fig. 1d**). The slope of the aspiration curve at the
102 point of constant flow depends on the viscosity η, $L_{asp} = R_p (\Delta P - P_c) / 3\pi\eta$ with R being the
103 radius of the pipette, ΔP the applied pressure and P_c the critical pressure. When the
104 pressure is set to zero during the relaxation, the tissue retracts at a velocity $L_{ret} = R_p (P_c) /$
105 $3\pi\eta$. From the aspiration and retraction rates, viscosity can be calculated as $\eta = R_p \Delta P / 3 \pi$
106 ($L_{asp} + L_{ret}$). In case the retraction rates are very low, then the major determinant of viscosity
107 is the aspiration rate. Notably, although a faster relaxation would be expected for lower η
108 given that L_{ret} is inversely proportional to η, this is not detectable when comparing central
109 (low η) versus marginal (high η) blastoderm tissues at the onset of doming due to the very
110 low surface tension of the central tissue as judged by micropipette aspiration (calculated
111 with $\gamma = P_c / 2R_p$; **Supplementary Fig. 1e**). Notably, the actual surface tension of deep cells
112 within the blastoderm is even lower than the surface tension measured by micropipette
113 aspiration, considering that in the micropipette aspiration experiments, surface tension of
114 deep cells at their interface to the buffer within the pipette is analysed, while within the
115 blastoderm, deep cells are not completely surrounded by fluid, but also form cell-cell
116 contacts with the EVL and yolk cell (see also CellFIT-3D analysis and **Supplementary Note**).
117
118 **3D-VFM/CellFIT-3D analysis**

To obtain the relative distribution of interfacial tensions of host and donor deep cell tissues in the transplantation experiments, the angles at triple edges between host (labelled by membrane-GFP), donor (labelled by membrane-RFP) and interstitial fluid (labelled by dextran Alexa Fluor 647) were digitized along multiple images from confocal z-stacks (3 µm interval) in transplanted embryos using custom software as described [40,57,58]. Force balance equations were written for each digitized triple edge and least-squares solutions were found for all equations. The solutions of these equations provided the relative interfacial tensions along each edge type.

Validation of 3D-VFM/CellFIT-3D analysis

To clarify that 3D video force microscopy (3D-VFM) is a valid method for measuring interfacial tension within the embryo, tissue surface tension (TST) of marginal and central deep cell tissues obtained by using either 3D-VFM or micropipette aspiration (MPA) were compared. When using MPA, the TST of the probed deep cell tissue at its interface to the buffer within the pipette is measured. In contrast, when using 3D-VFM in intact and internal tissues, the TST of the probed deep cell tissue at its interfaces with both medium and other surrounding cells is measured. In order to provide a common and thus comparable interface of the probed tissues in both the MPA and 3D-VFM measurements, marginal and central deep cell tissues for the 3D-VFM measurements were placed in culture medium/buffer, thereby mimicking the situation in the MPA measurements where the probed tissue faces the buffer in the micropipette. In such comparable conditions, the relative TST of marginal versus central deep cell tissues obtained by either 3D-VFM or MPA assays were similar (**Figure 2 of Supplementary Note**), supporting the notion that 3D-VFM can be used to measure TST within the embryo.

Immunostaining

Embryos were fixed in 2% paraformaldehyde (PFA) for 4 h at RT. After fixation, they were washed in 0.5% Tween-20 (in 1x PBS) overnight at 4^{o}C, dechorionated and washed in 0.5% Tween-20, 0.5% Triton X-100, 0.1 M glycine (in 1x PBS) for 1 h at RT. Embryos were then incubated in blocking solution (0.5% Tween-20, 0.5% Triton X-100, 1% DMSO, 1% BSA in 1x PBS) for 3-4 h at RT and then incubated with the primary antibody (rabbit E-cadherin anti-zebrafish [52], 1:200, generated at MPI-CBG) diluted in the blocking solution overnight at 4^{o}C. Embryos were subsequently washed 4 x 20 min in 0.5% Tween-20 and incubated with the secondary antibody (goat Alexa Fluor 546 anti-rabbit, 1:500, A11010 ThermoFisher Scientific) and Phalloidin Alexa Fluor 488 (1:500, A12379, ThermoFisher Scientific) diluted in the blocking solution overnight at 4^{o}C. Last, embryos were washed 4 x 20 min in 0.5% Tween-20, post-fixed in 4% PFA for 30 min at RT and imaged.

Image Acquisition

Dechorionated embryos were mounted in 0.5% low melting point agarose (16,520-050, Invitrogen) on a glass bottom dish (P35G-1.5-14-C, MatTek Corporation). Mounted embryos were kept in an incubation chamber at 28.5 ^{o}C throughout acquisition. Whole embryo single plane bright-field/fluorescence imaging was performed on a Nikon Eclipse inverted wide-field microscope equipped with CFI Plan Fluor 10x/0.3 objective (Nikon) and a fluorescent light source (Lumencor). For high magnification confocal imaging of deep cells, a Zeiss LSM880 inverted microscope, equipped with a Plan-Apochromat 40x / NA 1.2 water-immersion objective (Zeiss), a Plan-Apochromat 63x / NA 1.4 oil-immersion objective (Zeiss), GaAsP and multialkali PMT detectors and Fast Airyscan super-resolution was used. For

imaging the micropipette aspiration experiments, a Leica SP5 inverted microscope equipped with a resonant scanner and a HC Plan-Apochromat 10x/ NA 0.4 objective (Leica) was used.

Data analysis and quantification

All acquisition data were processed using Fiji (NIH), ilastik and/or imaris 9.0. EVL spreading (**Fig. 1c**) was measured as h_b/h_t, with h_b, height of the blastoderm from the top region of the embryo to the meeting point of EVL, BYI and yolk (as described in [19]) and h_t, total height of the embryo. This ratio was calculated every 5 min. BYI displacement was quantified as schematized in **Fig. 1d**. Specifically, the position of the BYI at sphere stage was set to zero. Using the multi-point tool in Fiji, the position of the BYI in each time point (6 min interval) was marked on the Y-axis in the centre (positive displacement) and at the margins (negative displacement, measured at 50 µm distance from the EVL margin). In the deep cell transplanted embryos, central BYI displacement was quantified in a similar manner, selecting a point on the BYI positioned below the central transplant. Marginal BYI displacement was measured in a region entirely consisting of non-transplanted host marginal cells. In the bead transplantations, central BYI displacement in the non-transplanted (control) and transplanted sides was measured in the same embryo as schematized in **Supplementary Fig. 2d**. For quantifying marginal BYI displacement in the bead-transplanted embryos, the margin at the bead-transplanted side was considered as 'bead marginal BYI', while the other side was considered as the 'control marginal BYI'. Tissue thinning was quantified as schematized in **Fig. 1e**. Blastoderm thickness in the centre of the embryo was measured as h_c/h_t, with h_c, height of the blastoderm in the centre (indicated by the red double-headed arrow from the centre top region of the embryo to the BYI) and h_t, total height of the embryo (extending the same arrow to the bottom of the yolk cell). This

ratio was calculated every 5 min. The shape of the BYI at dome stage in the marginal transplantation experiments was evaluated as shown in the diagram of **Supplementary Fig. 6f**. The angle formed between the marginal and central tissue was measured by drawing to virtual lines, one originating at the contact point of marginal EVL and BYI and extending along the BYI until the BYI changed direction, and one from the point the BYI changed direction and extending along the BYI new direction. Deep cell protrusion orientation relative to the radial axis of the blastoderm was quantified as schematized in **Supplementary Fig. 1a** and Actin intensity was measured in an ROI at the cell edges intersecting the radial or lateral axis. The percentage of cell divisions within the deep cell layer was determined by dividing the number of dividing deep cells by the total number of deep cells in 2D at the indicated time points. Relative interstitial spaces labelled by dextran Alexa Fluor 647 were quantified on confocal images of the first four deep cell layers of the blastoderm within central and marginal blastoderm regions (**Supplementary Fig. 3a**). A ROI of the same size for both regions and for each cell layer was selected, and using ilastik to segment interstitial fluid from cells, an intensity threshold was automatically determined for each image. This threshold was then used in Fiji to create a binary image, where the percentage of pixels above this threshold was considered as fluid and below as cells. For each cell layer, the interstitial fluid percentage was normalized to that at the onset of doming. Cell-cell contact time was quantified as follows: neighbouring deep cells from embryos labelled for membrane and interstitial fluid were followed over time (3 min interval) until deep cell-cell contact disassembly was identified by the presence of interstitial fluid between the cells. The total contact time was expressed as a percentage of the total recording time for each stage (~30 min). In the transplanted embryos, only the contacts between the donor deep cells were analysed. Cell-cell contact length was quantified as

follows: the contact length of neighbouring membrane labelled deep cells was normalized to the average cell diameter of the contacting cells. Contact length was defined by the length of the cell-cell interface free of interstitial fluid. Cell-cell contact length analysis was performed in a 3 min time interval. In the transplanted embryos, only the contacts between the donor deep cells were analysed. Cell-cell contact number was defined on 2D confocal images where the nuclei, cell-cell contacts and interstitial fluid accumulations were differentially labelled. Cell nuclei of cells within the same focal plane that had no interstitial fluid between them were considered as contacting cells. To extract the average contact number per cell, the number of contacts was divided by the total number of cells in the image. Notably, the average number of contacts per cell appears less than what is shown on the image due to the fact that the shared contacts are counted only once. To estimate deep cell-cell cohesion in **Fig.7,** the average number of contacts was multiplied with the average contact time and average contact size of central deep cells at high, sphere, onset, dome and 50% epiboly stages. For the distribution of adhesion proteins at the cell-cell contact, the images were first processed using the Airyscan mode (Zeiss). 3D reconstructions and cross-sections of the contact surface were performed by Imaris 9.0. The intensity profiles of E-cadherin and Actin at the contact surface were made using the line tool of 20 pixels' thickness in Fiji. The intensity values for the proteins shown were normalized to the maximum intensity value across each contact. For quantifying the clustering of deep cells around E-cadherin coated beads, interstitial fluid accumulation was measured as shown in **Supplementary Fig. 2a**. The average intensity of the interstitial fluid (labelled with dextran Alexa Fluor 647) was measured in ROIs (with an approximate width the size of a cell diameter) directly adjacent and further away (50 μm) from the bead. Mitotic rounding was quantified by measuring the length to width ratio (aspect ratio) of interphase and

metaphase deep cells at the plane of the DNA. Contact length relative to the cell cycle phase was analysed as follows: the same contact was followed over time from the interphase of cell cycle 11 (3 min time interval) onwards and the contact length was measured as described above for the following time points: 9 min before metaphase (t_{bm}), at metaphase (t_m) and 9 min after metaphase (t_{am}) from cycle 11 to 13. The data were normalized to the length of the contact at the first time point. For evaluating cell-cell contact disassembly in each cell cycle, the data were normalized to the length (L) of the contact at t_{bm} and disassembly (D) was expressed as $D = L_{bm} - L_m$. For evaluating the effect of cell cleavage on contact size for each cell cycle, the data were normalized to the length of the contact at t_{bm} and reassembly (R) was expressed as $R = L_{am} - L_{bm}$.

Statistical analysis

The statistical analyses were performed with GraphPad Prism. Statistical details of experiments are reported in the figures and figure legends. Sample size is reported in the figure legends and no statistical test was used to determine sample size. The biological replicate is defined as the number of embryos or independent batches of embryos, as stated in the figure legends. No inclusion/exclusion or randomization criteria were used and all analysed samples are included. Unless differently stated in the figure legends, the graphs show mean $\pm$ s.e.m and the error bars are calculated and shown based on the number of cells or embryos, as indicated. The statistical test used to access significance is stated in the figure legends and was chosen after testing each group with the normality distribution test D'Agostino. For comparing two groups, a two-tailed Student's t-test for parametric distributions and a Mann-Whitney u-test for non-parametric distributions were used. To compare more than two groups either an ANOVA or Kruskal-Wallis test for parametric and

non-parametric distributions, respectively, was used. Statistically significant differences are: * $P < 0.05$; ** $P < 0.01$; *** $P < 0.001$; **** $P < 0.0001$. No blind allocations were used during the experiments or in the analysis. All statistical analysis detailed are reported in **Statistics source data.**

Data availability

The Fiji macro used to quantify the micropipette aspiration experiments is available upon request. The data supporting the findings of this study and simulations are available from the corresponding author upon request. The coordinates of the interfacial tension vectors and a script to back-track the angles from the 3D-VFM analysis are available upon request. The associated raw data for all figures is provided in the statistics source data.

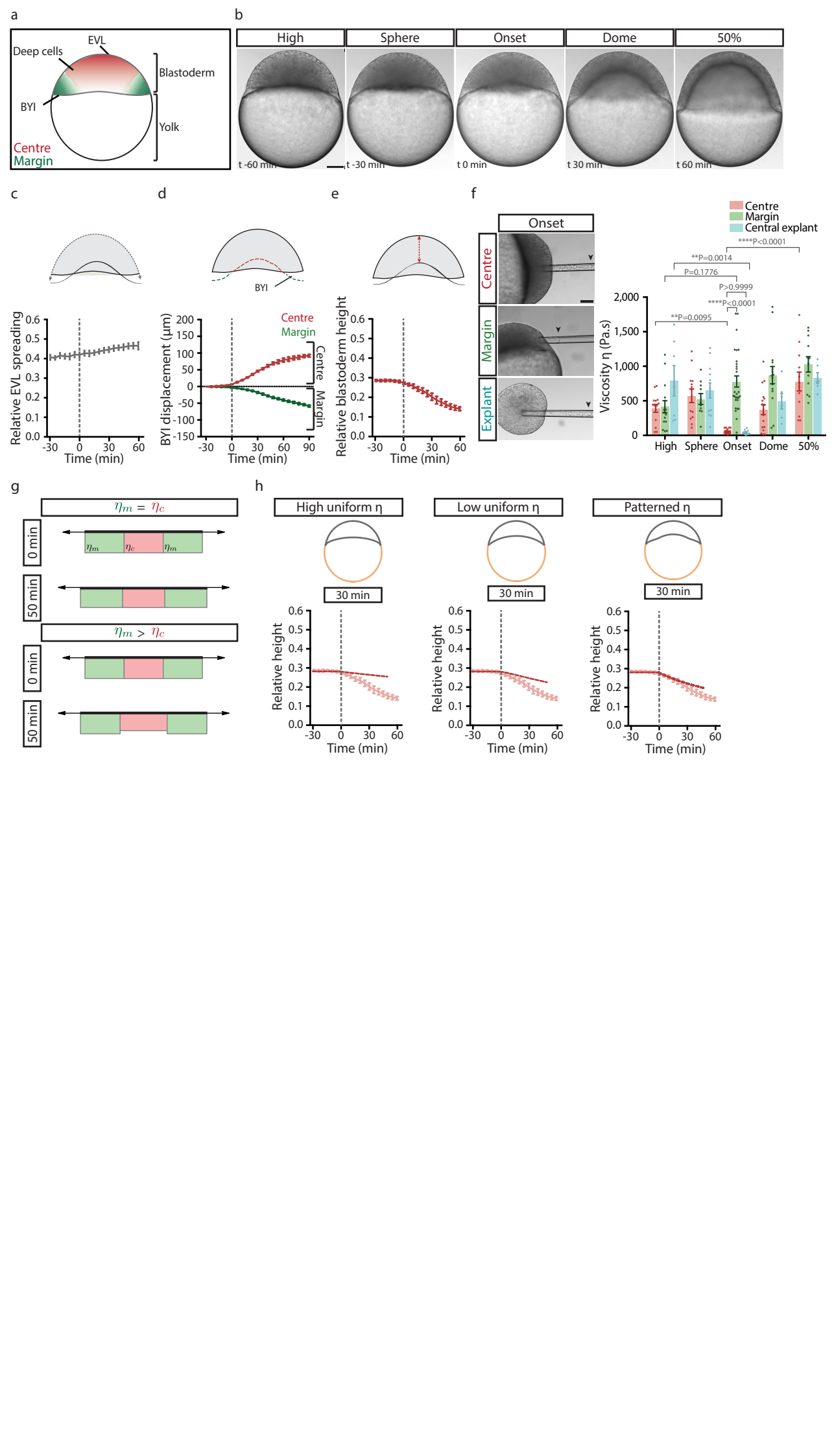
a
EVL
Deep cells
Blastoderm
BYI
Yolk
Centre
Margin
b
High
Sphere
Onset
Dome
50%
t -60 min
t -30 min
t 0 min
t 30 min
t 60 min
c
Relative EVL spreading
Time (min)
d
BYI
BYI displacement (µm)
Centre
Margin
Time (min)
e
Relative blastoderm height
Time (min)
f
Onset
Centre
Margin
Explant
Centre
Margin
Central explant
Viscosity η (Pa.s)
****P<0.0001
**P=0.0014
P=0.1776
P>0.9999
****P<0.0001
**P=0.0095
High
Sphere
Onset
Dome
50%
g
$\eta_m = \eta_c$
0 min
50 min
$\eta_m > \eta_c$
0 min
50 min
h
High uniform η
Low uniform η
Patterned η
30 min
Relative height
Time (min)

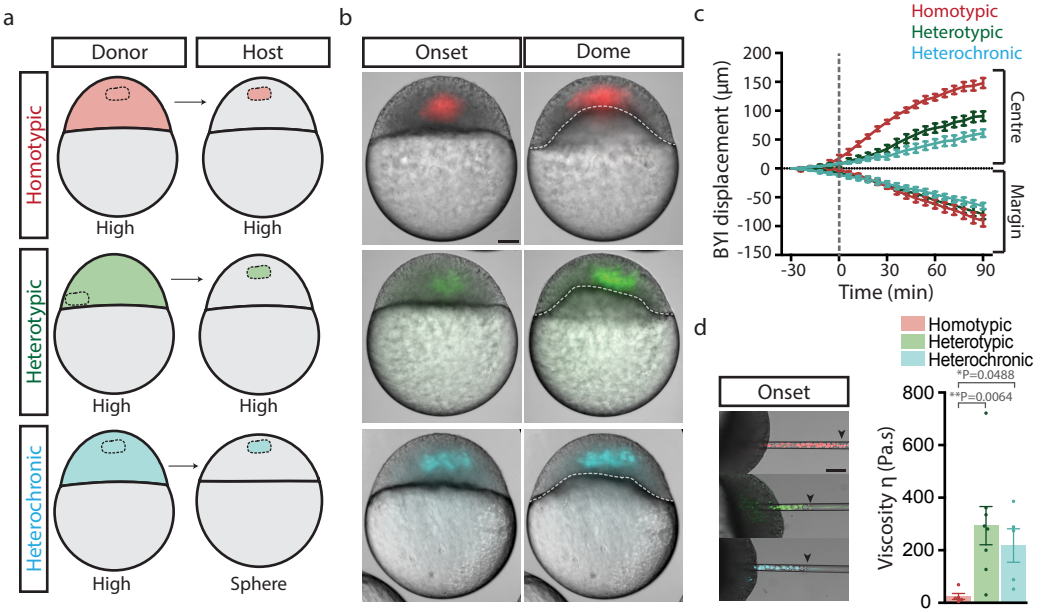
a
Donor
Host
Homotypic
High
High
Heterotypic
High
High
Heterochronic
High
Sphere
b
Onset
Dome
c
Homotypic
Heterotypic
Heterochronic
BYI displacement (µm)
200
150
100
50
0
-50
-100
-150
Centre
Margin
-30
0
30
60
90
Time (min)
d
Onset
Homotypic
Heterotypic
Heterochronic
*P=0.0488
**P=0.0064
Viscosity η (Pa.s)
800
600
400
200
0

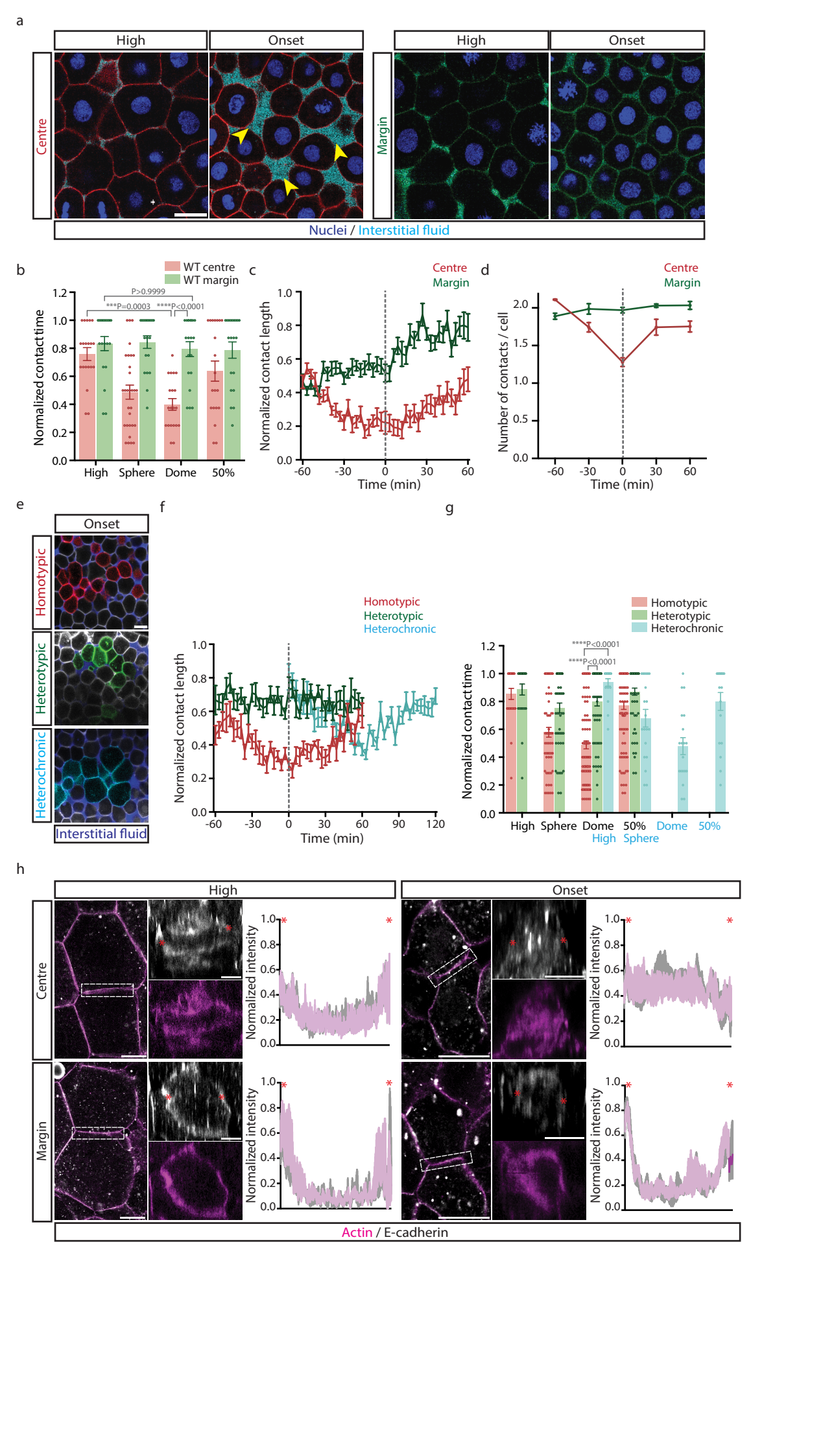
a
High
Onset
High
Onset
Centre
Margin
Nuclei / Interstitial fluid
b
WT centre
WT margin
P>0.9999
***P=0.0003
****P<0.0001
Normalized contact time
High
Sphere
Dome
50%
c
Centre
Margin
Normalized contact length
Time (min)
d
Centre
Margin
Number of contacts / cell
Time (min)
e
Onset
Homotypic
Heterotypic
Heterochronic
Interstitial fluid
f
Homotypic
Heterotypic
Heterochronic
Normalized contact length
Time (min)
g
Homotypic
Heterotypic
Heterochronic
****P<0.0001
****P<0.0001
Normalized contact time
High
Sphere
Dome
50%
High
Sphere
Dome
50%
h
High
Onset
Centre
Margin
Normalized intensity
Actin / E-cadherin

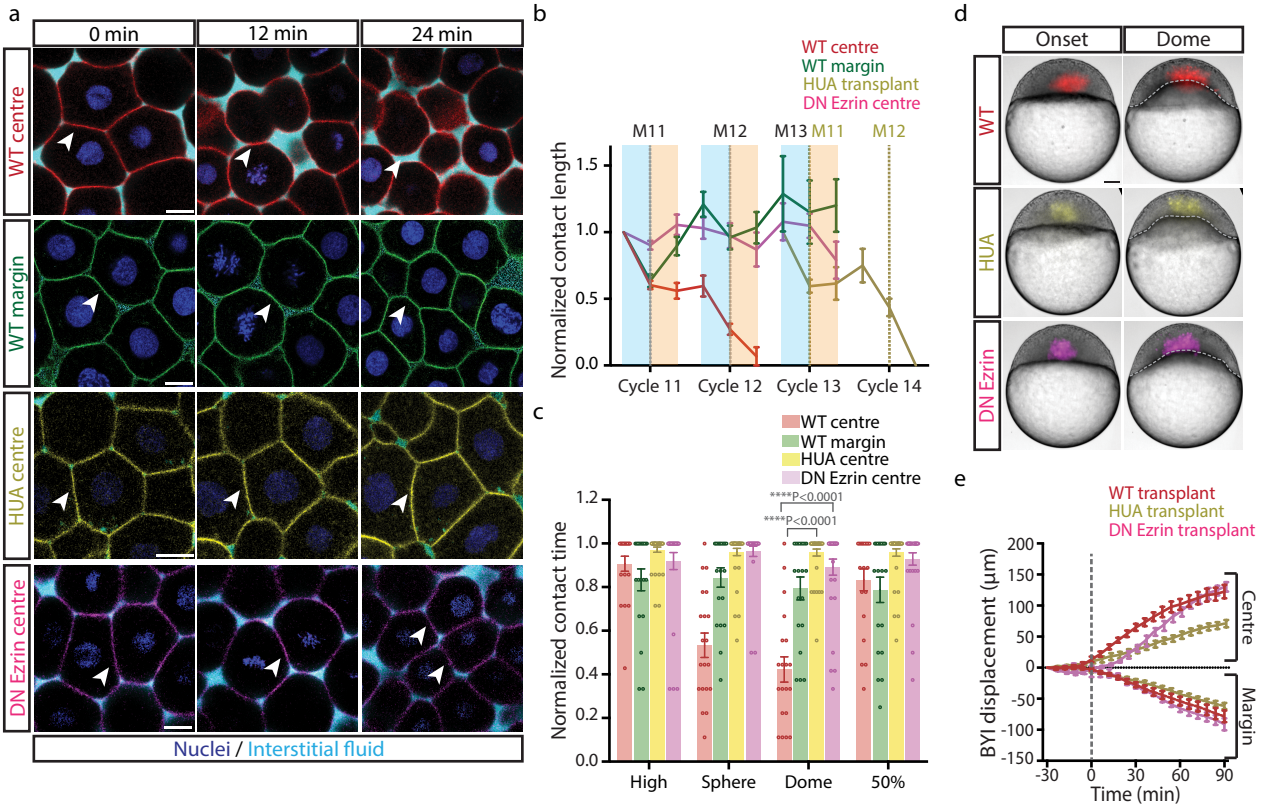
a
0 min
12 min
24 min
WT centre
WT margin
HUA centre
DN Ezrin centre
Nuclei / Interstitial fluid
b
WT centre
WT margin
HUA transplant
DN Ezrin centre
M11
M12
M13
M11
M12
Normalized contact length
1.5
1.0
0.5
0.0
Cycle 11
Cycle 12
Cycle 13
Cycle 14
c
WT centre
WT margin
HUA centre
DN Ezrin centre
****P<0.0001
****P<0.0001
Normalized contact time
1.2
1.0
0.8
0.6
0.4
0.2
0.0
High
Sphere
Dome
50%
d
Onset
Dome
WT
HUA
DN Ezrin
e
WT transplant
HUA transplant
DN Ezrin transplant
BYI displacement (µm)
200
150
100
50
0
-50
-100
-150
Centre
Margin
-30
0
30
60
90
Time (min)

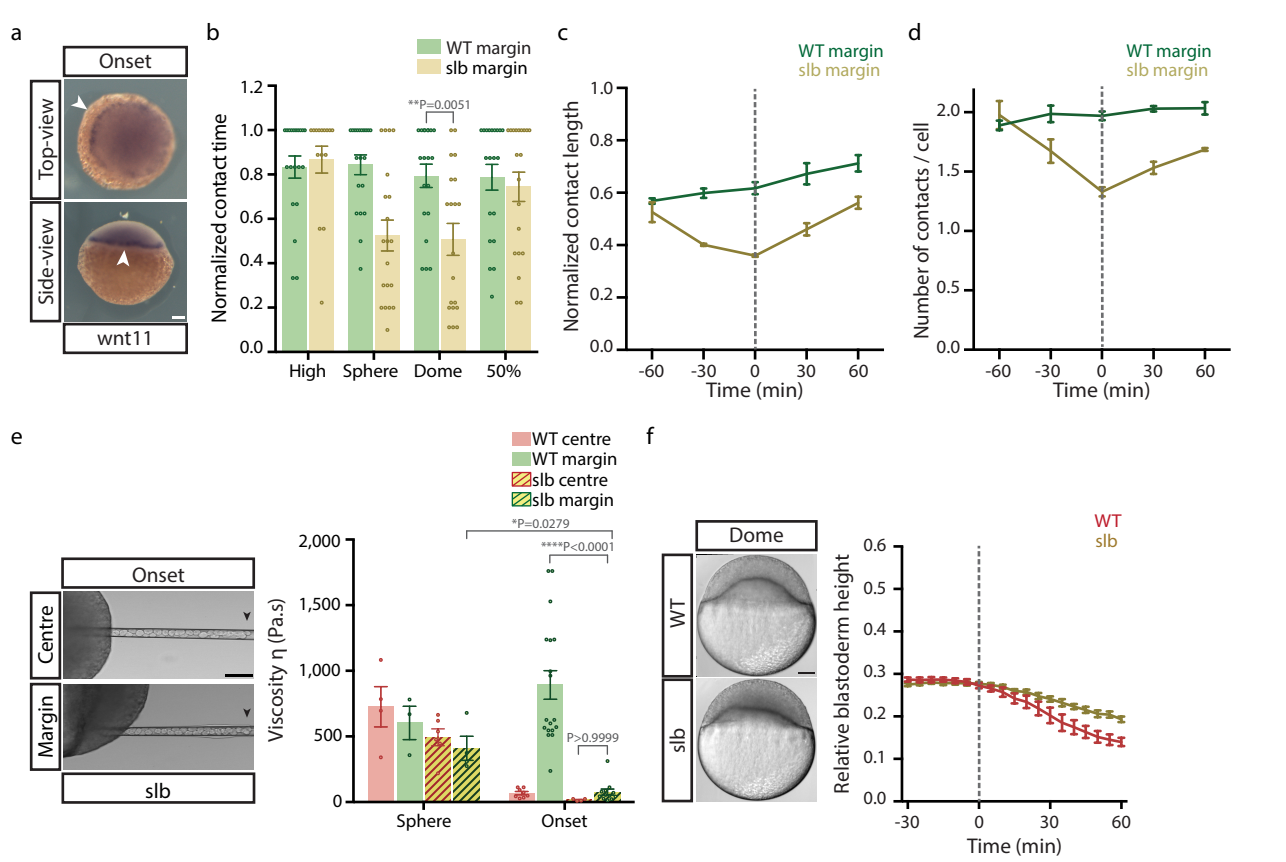
a
Onset
Top-view
Side-view
wnt11
b
WT margin
slb margin
Normalized contact time
**P=0.0051
High
Sphere
Dome
50%
c
WT margin
slb margin
Normalized contact length
Time (min)
d
WT margin
slb margin
Number of contacts / cell
Time (min)

e
WT centre
WT margin
slb centre
slb margin
Onset
Centre
Margin
slb
Viscosity η (Pa.s)
*P=0.0279
****P<0.0001
P>0.9999
Sphere
Onset
f
Dome
WT
slb
WT
slb
Relative blastoderm height
Time (min)

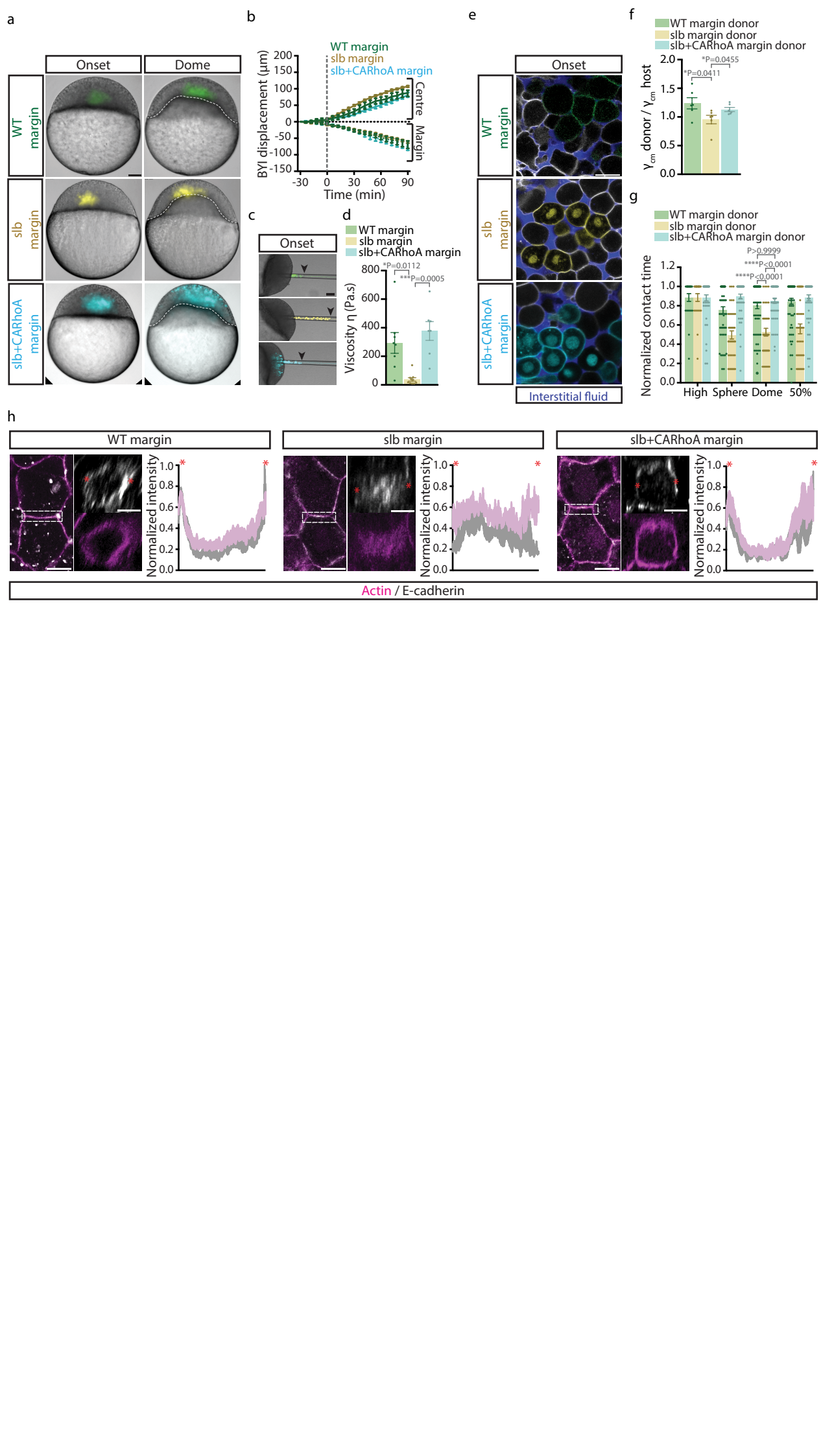
a
Onset
Dome
WT margin
slb margin
slb+CARhoA margin
b
WT margin
slb margin
slb+CARhoA margin
BYI displacement (µm)
Centre
Margin
Time (min)
c
Onset
d
WT margin
slb margin
slb+CARhoA margin
*P=0.0112
***P=0.0005
Viscosity η (Pa.s)
e
Onset
WT margin
slb margin
slb+CARhoA margin
Interstitial fluid
f
WT margin donor
slb margin donor
slb+CARhoA margin donor
*P=0.0455
*P=0.0411
γcm donor / γcm host
g
WT margin donor
slb margin donor
slb+CARhoA margin donor
P>0.9999
****P<0.0001
****P<0.0001
Normalized contact time
High
Sphere
Dome
50%
h
WT margin
slb margin
slb+CARhoA margin
Normalized intensity
Actin / E-cadherin

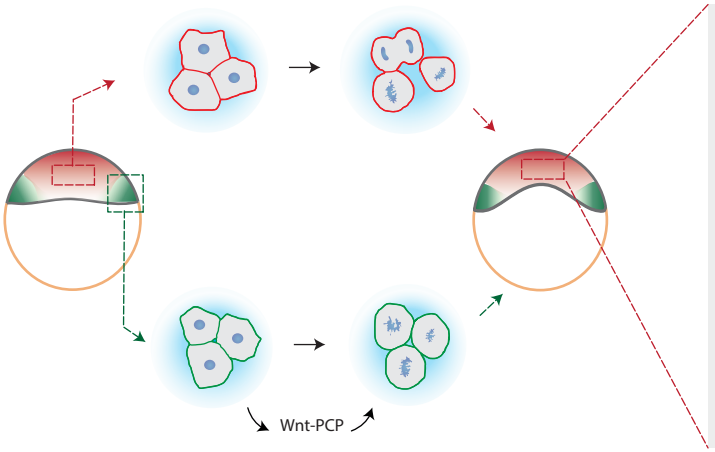
Wnt-PCP

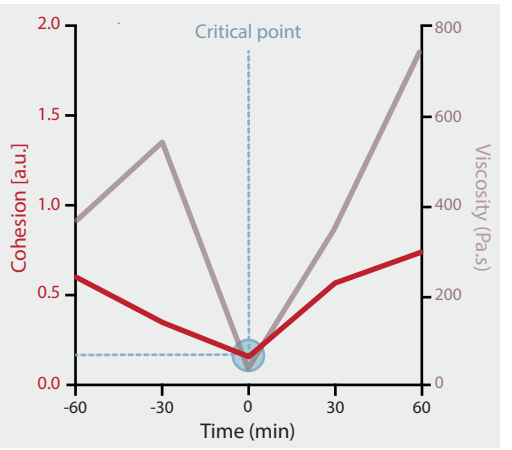
Critical point
Cohesion [a.u.]
Viscosity (Pa.s)
Time (min)
2.0
1.5
1.0
0.5
0.0
800
600
400
200
0
-60
-30
0
30
60